Fabrication artifacts and parallel loss channels in metamorphic epitaxial aluminum superconducting resonators

C. J. K. Richardson[1], N. P. Siwak[1], J. Hackley[1], Z. K. Keane[1], J. E. Robinson[1], B. Arey[2], I. Arslan[2], B. S. Palmer[1,3]

[1] Laboratory for Physical Sciences, University of Maryland, 8050 Greenmead Dr., College Park MD 20740
[2] Fundamental and Computational Science Directorate, Pacific Northwest National Laboratory, Richland, Washington 99352, United States
[3] Department of Physics, University of Maryland, College Park, Maryland 20742, USA

E-mail: `richardson@lps.umd.edu`

December 14, 2015

Abstract. Fabrication of coplanar waveguide resonators with internal quality factors near 10^6 remains challenging. Here, high-purity single crystal superconductors are implemented through metamorphic epitaxial aluminum that is grown via molecular beam epitaxy on silicon and sapphire substrates. X-ray diffraction and scanning transmission electron microscopy indicate an abrupt highly ordered interface that results in crystal relaxation within a few monolayers of the substrate interface and no measurable interfacial contamination. Quarter-wave coplanar waveguide resonators are fabricated using optical lithography and measured at temperatures below 100 mK. Post measurement characterization with charge contrast imaging in a scanning electron microscope identifies processing artifacts at the waveguide sidewalls, on the exposed substrate area and on the exposed aluminum surface. Of primary importance are processing induced corrosion defects on aluminum sidewalls, nanoparticle contamination, and photoresist residue that is difficult to remove without affecting the superconductor material. Likely correlations between these artifacts and the measured quality factor are discussed in context of device to device variations in resonator performance.

PACS numbers: 74.70.Ad, 74.78.Fk

Keywords: Aluminum, Superconductor, Resonator, Loss, Residue

Submitted to: *Supercond. Sci. Technol.*

1. Introduction

With the implementation of circuit quantum electrodynamic (cQED) architectures, the ability to fabricate planar resonators with microfabrication technologies is a critical technology necessary to produce high coherence quantum circuits on a chip. Circuit quantum electrodynamic architectures couples a resonator to a Josephson junction qubit to produce a qubit system. [1]. Therefore, improvements in the resonator lifetime directly contributes to a more stable qubit system. A number of on-chip resonators have been successfully implemented in this fashion [2–4].

The practical limit to cavity lifetimes of on chip resonators is ultimately defined by the microwave loss of the microwave waveguide or lumped circuit components. In addition to quantum information technologies, extremely low microwave loss on-chip resonators are also a critical characteristic of superconducting single photon detectors [5].

The quality factor, Q, of two-dimensional resonators as a function of temperature and applied microwave power have been studied by numerous groups. Several reports focus on comparisons of materials that can be produced with internal quality factors greater than 10^6. Consolidated studies of different superconductor and substrate materials used in coplanar waveguide resonators show large variations [6]. Comparison of the deposition technology used to produce the superconductor film has shown that higher purity processes produce higher-Q resonators [7].

Complementing these studies that measure waveguide resonators, examination of the loss associated with dielectric materials deposited in a parallel plate geometry show material trends related to deposited dielectrics that may be used as the insulating barrier in Josephson junctions or isolating wire cross-over bridges necessary for more complicated circuits [8, 9].

To date, coplanar waveguide resonators made from epitaxial aluminum and titanium nitride have demonstrated quality factors in excess of 10^6 at applied powers that are applicable to use in quantum information systems. However, trends have emerged that thin interfacial layers, such as the native oxide on silicon, can impact the resonator performance [10], and specific process steps can also directly impact microwave loss [11, 12]. Numerical studies have shown that trench etching into the substrate affects the electric field distribution [13] and that the superconductor/substrate interface, in addition to the center conductor sidewall of a co-planar waveguide are specific areas of great sensitivities to loss resulting from thin layers of lossy material. Several approaches to manipulating the coplanar gap geometry have been implement and shown to impact resonator performance [14, 15].

Dielectric loss has been identified as a leading source of microwave loss in superconductor waveguide resonators. This dielectric loss is described in the abstract context of a quantum two level system (TLS) that resonantly couples to the microwave energy. The energetic description of two local potential minima that are sufficiently close to allow tunneling was originally described for bulk amorphous materials [16]. More recent connections of a broad distribution of TLS defects contributing to loss in waveguide resonators have been made [17–19]. Density functional theory (DFT) has been used to connect possible microscopic origins of oxygen vacancies [20], or interstitial hydrogen impurities [21] to TLS loss in bulk Al_2O_3.

Here, aluminum is used as the superconducting material of study because of its extensive use in the quantum computing community as passive interdigitated capacitors, meandering inductors, transmission lines, and Josephson junctions. Having a two-dimensional sheet of potentially very low loss material and a consistent superconductor/substrate interface is a critical foundation that is needed to explore variations in loss that may result from processing artifacts and fabrication variations of the tested waveguides. With the goal of producing such an interface, low loss substrates of silicon and sapphire are extensively cleaned before high-purity growth protocols associated with molecular beam epitaxy (MBE) are applied to the deposition of 100-nm thick aluminum. As a result of these procedures a relaxed single crystal aluminum film is grown that exhibits a highly ordered and abrupt metamorphic epitaxial interface. With the entropic perspective that contamination and loss will increase during device fabrication, the bulk and interfacial structure of these materials are described for context to the field, while detailed analysis of the interface is considered outside the scope of this article. The measurement and analysis techniques are described to identify resonator performance and specific device defects that may correlate with microfabrication process variations.

Interest in epitaxial superconductors extends beyond their use as low-loss passive materials in cQED experiments. Thin epitaxial superconductors grown on semiconductor substrates and nanowires are of interest to study proximity affects; such as spin-orbital superconductivity interactions [22–24] between superconductor nanofilms on III-V substrates, and the proximity-induced superconductivity of aluminum on InAs nanowires [25]. The later having been implemented as a voltage tunable Josephson junction in a cQED qubit devices [26].

2. Resonator Assessment

The measurement and analysis of quarter-wave microwave coplanar resonators follows conventional approaches, [27, 28] which is summarized here for completeness. That is, the complex transmission of the devices are measured in one of three cryogenic systems. Two systems are dilution refrigerators that have been used to perform spectroscopy of numerous qubit devices, [29, 30] and the third is an adiabatic demagnetization refrigerator that is set-up following the designs of Barends, *et al.* [31].

The frequency resolved complex ratio of the transmitted voltage to the input voltage, $S_{21}(f)$, around the resonance frequency, f_o, is modeled using a description that allows for complex coupling of the resonator to the waveguide, and incomplete path length compensation:

$$\tilde{S}_{21}(f) = e^{i(\theta+\kappa L)}\left[1 - \frac{Q_T\left(Q_C e^{i\phi}\right)^{-1}}{1 + 2iQ_T\left(\frac{f-f_o}{f_o}\right)}\right]. \qquad (1)$$

The observed total quality factor, $Q_T^{-1} = Q_C^{-1} + Q_I^{-1}$ is determined by the coupling quality factor Q_C, and the internal quality factor Q_I. Determination of the various parameters is completed in both parametric and complex spectral transmission modalities as fitting benefits from both perspectives towards creating a robust analysis method. Initial fitting of the parametric description using a geometric Taubin fit of S_{21} allows for fitting of the coupling phase, ϕ, resonator phase angle, θ, path length compensation, κL, and initial estimates of the resonance frequency, and quality factors Q_T and Q_C. These values are used as the starting points for the linear least square fit of the real or imaginary components of $S_{21}(f)$ where accurate determination of the values and uncertainty of f_o, Q_C, and Q_T are found and used to determine the internal quality factor within a framework that enables error analysis.

A simulated image of the electric field magnitude in the folded, shunted, quarter-wave, coplanar waveguide is shown in figure 1(a). In the panels to the right, representative resonator data (blue dots) and fit (red line) results of one resonator are shown in both the parametric plot (figure 1(b)), magnitude (figure 1(c)) and phase (figure 1(d)) of S_{21}.

Measurement of the complex transmission through these devices are completed with a range of applied RF power with the goal of observing saturable absorption related to TLSs [6, 19]. The loss tangent of dielectric loss is often associated with resonant two-level defects with a power dependence described as $\tan(\delta) = \tan(\delta_{TLS})[1 + (n/n_c)]^{-1/2}$, where $\tan(\delta_{TLS})$ is the magnitude of the loss tangent associated with the resonant coupling of the defect states and the quantum device states; n, is the excited state population that is related to the magnitude of the applied driving field that couples with the dipole moment of the TLS defect; and n_c is the critical number that defines the saturation of the TLS defects. Descriptions that express this saturation behavior in terms of the number of photons stored in the resonator, or the local electric field can be written in similar forms. The power dependent internal quality factor of five resonators with different center widths from one particular resonator chip fabricated on silicon using dry etch process detailed later is shown in figure 2.

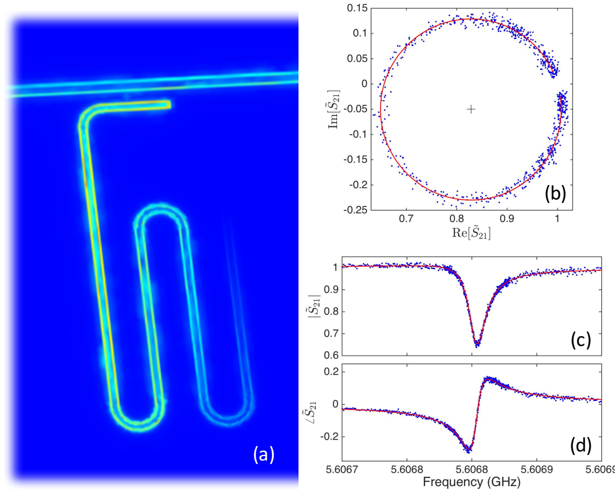

Figure 1. (a) Simulated electric field strength of a shunted quarter-wave coplanar waveguide resonator. The resonator is capacitively coupled to a coplanar bus waveguide running horizontally across the simulation near the top of the figure. Measured S_{21} (points) and fit (line) from one resonator is shown in the (b) parametric representation and the (c) magnitude and (d) phase in the spectral representation.

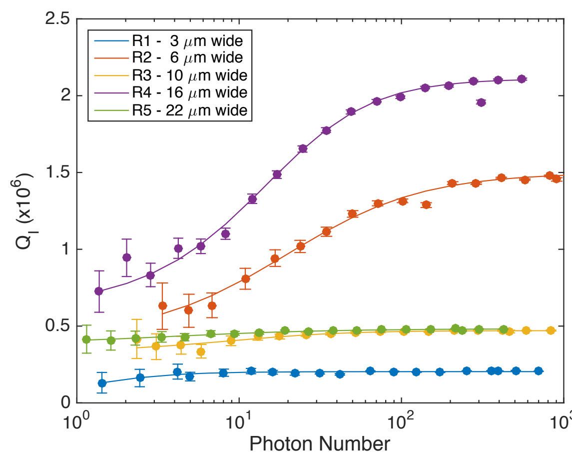

Figure 2. Power dependence of the internal quality factor for five resonators fabricated on a single chip.

Of immediate notice are the different power dependencies for each resonator. These trends are representative of normal variations seen on nearly every chip that is processed and measured. There are two practical considerations that cause this relationship regarding the applied microwave power to not be observed. The first is the contribution from a number of parallel loss channels. That is, the internal quality factor is the sum of all contributions, *i.e.* $(Q_I^{-1})_{total} = \sum (Q_I^{-1})_i$. Often the inverse internal quality factor is equated to be the microwave loss tangent, *i.e.* $Q_I^{-1} = \tan(\delta)$. Here, the discussion is kept in terms of the inverse internal quality factor to explicitly acknowledge all forms of loss. Some of these loss mechanisms are linear (constant in power), such as loss from vortices [32] and loss from background stray fields and radiation from sub-wavelength waveguides [6].

One might expect that vortex and quasi-particle loss is likely to affect each resonator equally, and that radiation will depend on the size of the center conductor that ranges from 2 μm to 22 μm in the studied resonators. For this particular chip, resonators R2 and R4 are on one side of the chip transmission line, while resonators R1, R3, and R5 are on the other side. It is relatively direct reasoning that interprets the different behavior as an experimental variation that is not representative of the material or waveguide width, but is likely an indication of inconsistency in the fabrication process across the chip. Indeed, sometimes defect trends are found that correlate to variations in the observed loss trend such as this. Given this potential for variation, the power dependent loss including linear and saturable loss may be expressed in terms of the magnitude of the local electric field as

$$(Q_I^{-1})_{total} = (Q_I^{-1})_A + \sum_{ij} (Q_I^{-1})_i \left\{ 1 + \left[\frac{|E(x_j, y_j, z_j)|}{(E_c)_i} \right]^2 \right\}^{-1/2} \quad (2)$$

Where contributions from resonant TLS entities that may have different microscopic origins, designated with the subscript i, share a common dipole moment and therefore each type of TLS loss should have a common loss $(Q_I^{-1})_i$. It is assumed that the majority of TLS defects will not be strongly coupled to the cavity or other quantum states, allowing the spontaneous emission rate to be considered consistent across similar defects and will accordingly have a common critical field, $(E_c)_i$. For those TLS defects that do not satisfy this criteria, unique critical numbers will need to be assigned to each specific defect. For each individual defect, identified through the subscript, j the spatial variation of the electric field $E(x_j, y_j, z_j)$ that establishes the excited state population is not necessarily consistent between any two defects.

As shown graphically in figure 1(a) through finite element simulations of the electric field strength, the shunted quarter wave resonator has a node at the grounded end, and an antinode at the end that is capacitively coupled to the transmission waveguide. This results in a significant longitudinal variation in the electric field strength which results in different degrees of saturation based solely on the absolute physical location on the resonator. In the situation where there is more than one defect, the strong geometrical dependence of the local electric field encourages use of a phenomenological power dependence that is reasonably evaluated with a suitable empirical relationship. [33] The relationship used here is

$$(Q_I^{-1})_{total} = (Q_I^{-1})_A + (Q_I^{-1})_{sat} \left[1 + \left(\frac{|E|}{E_c} \right)^2 \right]^{-\alpha} . \quad (3)$$

This analysis is applicable to coplanar waveguide resonator devices that have strong field variations along the length of the resonator but may not need to be applied to other geometries such as parallel plate geometries where the electric field is considerably more uniform across a homogenous distribution of similar defects.

Table 1 summarizes the extracted loss parameters from several resonators fabricated using a variety of etch processes. The photoresist was removed using a short 5 second dip in FUJIFILM OPD 4262, a metal-ion-free tetramethylammonium hydroxide (TMAH) photoresist developer followed by ultrasonication and extensive soaks in hot N-methyl-2-pyrrolidone (NMP). All samples are made from epitaxial materials and results are presented for all five resonators that are fabricated on a single chip. Strong chip-to-chip variation have been observed in addition to the significant performance variations for neighboring devices reported in the table.

3. Superconductor growth

Detailed cross-sectional analysis of the electric field distribution indicates that the superconductor/substrate interface is one region where the electric fields are concentrated, and therefore more likely to generate loss through coupling to resonant defects with non-negligible dipole moments. En-route to creating the cleanest substrate surface on which to deposit the superconductor metal *ex-situ* chemical cleans are combined with ultra-high vacuum (UHV) *in-situ* thermal treatments.

The process for growth on commercial (0001) oriented edge-defined film-fed growth sapphire wafers begins with an initial degrease prior to introduction into an ultra-high vacuum (UHV) MBE system where water is desorbed at 150°C for a few hours. Additional

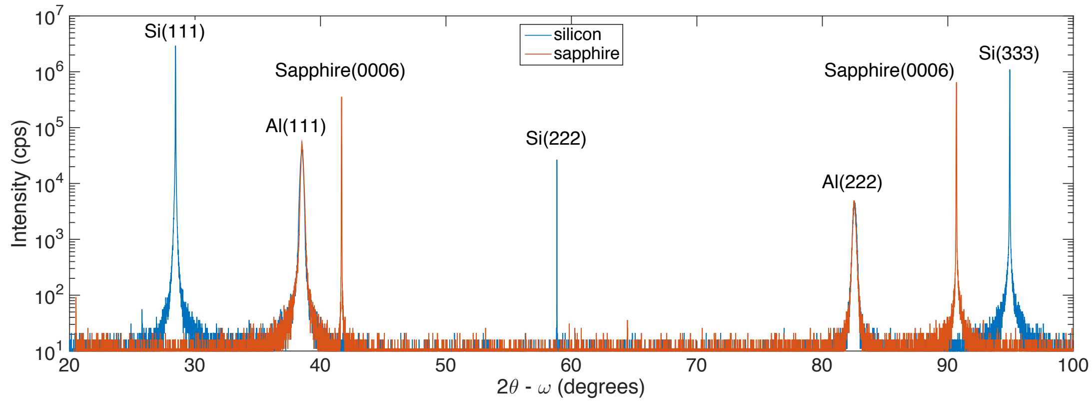

Figure 3. X-ray diffraction $\omega - 2\theta$ of two metamorphic single crystal aluminum samples grown on silicon (111) (shown in blue) and c-plane sapphire (shown in red).

Table 1. Low-photon number losses exhibit both linear loss representing an aggregation of sources, $(Q_I^{-1})_A$, empirical TLS loss, $(Q_I^{-1})_{sat}$, with a saturation photon density (n_c) for 50 Ω coplanar waveguide resonators of various center widths (w).

Sample	w (μm)	$(Q_I^{-1})_A$ ($\times 10^{-6}$)	$(Q_I^{-1})_{sat}$ ($\times 10^{-6}$)	n_c
Silicon (111) Wet-etch	3	0.0	4.3	2.4
	6	1.0	1.4	64
	10	0.8	760	0.0
	16	21	3.5	6200
	22	5.8	0.2	107
Silicon (111) Dry-etch	3	4.9	4800	0.0
	6	0.7	1.7	6.2
	10	2.1	0.9	9.4
	16	0.5	1.1	8.0
	22	2.1	0.5	0.3
Sapphire (0001) Dry-etch	3	1.6	1.5	27
	6	0.6	2.6	1.3
	10	1.3	7.4	0.0
	16	0.8	2.1	15000
	22	0.5	0.4	6500
Sapphire (0001) Wet-etch	3	0.0	2.2	2.7
	6	7.2	5.3	255
	10	2.6	5.2	0.2
	16	6.4	0.5	2100
	22	5.5	2.0	2.7

surface contamination is removed after transfer to the growth chamber where the substrate was heated to 850°C in a UHV environment that has a base pressure below 1x10^{-10} mbar. The sample is cooled to 140°C at which point ultra-high purity aluminum (>6N purity) is evaporated from a pyrolytic boron nitride crucible that is heated in a thermal effusion cell at a rate of approximately 0.25 Å/s

The process for growth on (111) orientated float-zone refined high-resistivity silicon is similar except that an *ex-situ* chemically etch is used to removed the native oxide with 5% HF followed by 40% NH_4F both for 1 min. The hydrophobic wafers are loaded into a UHV MBE system and the identical pre-growth UHV *in-situ* treatment is completed. During this process an optical pyrometer measures the wafer temperature to insure that the wafer surface exceed 750°C. The surface reconstruction is verified with reflection high energy electron diffraction to be 7x7, indicating a clean silicon surface following the desorption of the residual oxygen, flourine, and hydrogen [34]. All steps of this process are necessary to avoid growth of multiple crystal orientations that have been observed in past reports [35, 36].

All as-grown wafers are evaluation with x-ray diffraction, where a wide-angle $\omega - 2\theta$ symmetrical scan is used to identify the aluminum phases and orientation that are present. The well defined (111) diffraction peak of silicon and the (0006) diffraction peak of sapphire are used as calibration signals to correct for fine misalignment of the sample in the x-ray system. All wafers that are prepared with the described procedures consist of (111) single crystal aluminum that is crystallographically aligned with the substrate. Data from aluminum films grown on both silicon and sapphire wafers are shown in figure 3.

Apparent in figure 3 is the crystallographic alignment of the aluminum (111) peaks in both samples. This angle 38.43° agrees with the bulk (111) spacing of aluminum, indicating that the aluminum is completely relaxed on both substrates. The nominally 150 arcseconds FWHM of the aluminum peak is narrow, indicating that the relaxed aluminum film does not contain a strain gradient.

Further XRD analysis of these samples indicate that the aluminum films are highly oriented and twinned. Two examples of the twinned aluminum is shown in figure 4, where the diffractometer is

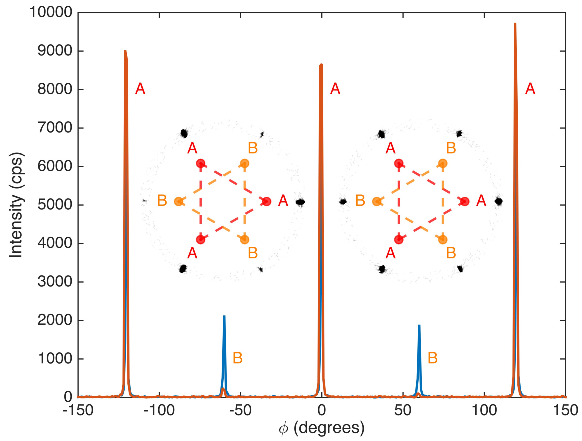

Figure 4. Unwrapped pole figure of x-ray diffracted intensities resulting from measurement of off-axis 111 aluminum planes. The inset polar figures present the intensities corresponding to complementary twin regions.

configured to measure the off-axis (111) aluminum planes and the sample is rotated around, ϕ, which is the rotation axis that is parallel with the surface normal. Face centered cubic materials such as aluminum should be three-fold symmetric in this measurement. The existence of a pair of three-fold symmetric patterns that are mirror images of each other are evident in the inset figures of 4. The 1 mm x 5 mm illumination area of the diffractometer enable the relative area fraction of the two orientations (designated A & B) to be estimated by the ratio of the diffracted intensity. As shown in the line graphs in figure 4 the relative intensities of the B/A twins vary from sample to sample ranging from 0 to 1. The twin ratios are independent of the substrate material on which they are grown and do trend with growth temperature, with twin ratios proportional to the growth temperature as measured in the 50°C to 300°C window. The existence of twins is not surprising because of sensitivity to surface contamination [35], annealing history [36], and surface reconstruction [37]. However, in contrast to unstructured grain boundaries, twin boundaries are highly oriented and extremely localized with few dangling bonds. They are therefore unlikely sources of enhanced diffusion of contaminants during device processing, nor likely to negatively impact the superconducting properties because of the relatively long coherence length of cooper pairs compared to the lateral extent of twin boundaries.

4. Superconductor - Substrate Interface

To directly image the superconductor/substrate interface and verify the absence of interfacial layers, two samples were examined with an aberration corrected scanning transmission electron microscopy (STEM). Both sample were prepared with focused ion beam (FIB) milling to an imaging thickness of approximately 50 nm. For the aluminum grown on silicon the cross-sectional sample for STEM is prepared such that the imaging beam propagates parallel to the $(1\bar{1}0)$ direction, while for the sapphire substrate material the sample was prepared for the electron beam to propagate in the $(10\bar{1}0)$ direction. Representative images are shown in figure 5.

The choice of substrate orientation was selected to allow aluminum to grow on a close packed plane. For imaging, the specific crystal directions of the samples were chosen such that the edge of one set of misfit dislocations can be imaged as a result of the electron imaging beam propagating down its length. These images indicate that there are no undesired species at the interface, amorphous interfacial layers, and that the strain is immediately relaxed within a few monolayers of the substrate interface.

The combined information from large area XRD and high resolution STEM indicate that the relaxed aluminum single crystal is an abrupt interface metamorphic material, where the strain relaxation occurs through a periodic array of misfit dislocations that are arranged at the aluminum/substrate interface whose spacing, S, is determined by the ratio of the magnitude of the Burger's vector to the misfit strain. For aluminum on silicon the misfit spacing is 1.1 nm, and for aluminum growth on sapphire the spacing is 5.6 nm. This spacing is evident in the illustrated portion of figure 5(a) as the distance between the red lines that represent the extra plane of aluminum atoms. Yellow lines are drawn on atomic planes that are not perfectly registered between the aluminum film and silicon substrate, and green lines are drawn to indicate the planes that are aligned. The misfit spacing is too large to fit into the field of view in figure 5(b). The presented magnification is selected to be identical for both panels in figure 5 and show the highly ordered interfaces.

It should be noted that for growth on silicon there is a thermal growth budget related to the formation of aluminum silicides. If the aluminum layer is grown at an elevated substrate temperature the aluminum significantly roughens as aluminum reacts and spikes into the silicon substrate. This reaction between aluminum and silicon is observed at temperature significantly lower than the eutectic temperature of 577.6°C most likely because of the excess thermal energy of the adsorbed aluminum that is evaporated from a molten source maintained near 1150°C.

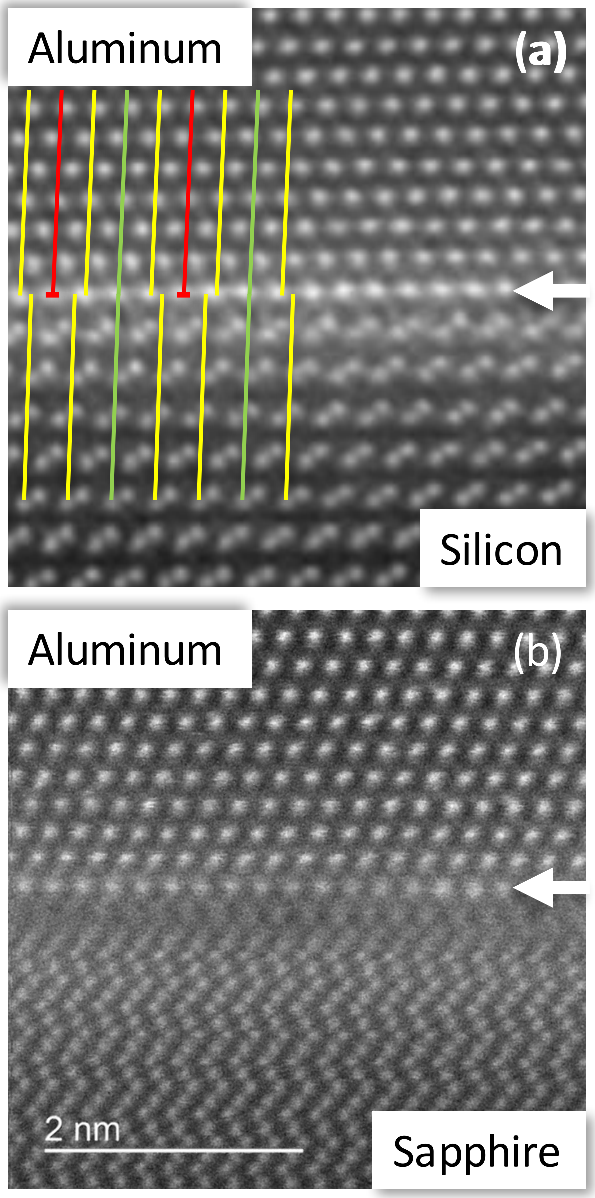

Figure 5. Atomic resolution scanning transmission electron microscopy of single crystal aluminum (111) grown on (a) silicon (111), and (b) sapphire (0001). Images are shown at similar magnification and scale. The arrow points to the first monolayer of the aluminum thin film. In the top image, red lines represent the extra plane of aluminum atoms, yellow lines on atomic planes that are not perfectly registered, and green lines are drawn to indicate the planes that are aligned.

5. Resonator fabrication

Resonators are fabricated through standard microfabrication processing using projection optical lithography and Novolac-based i-line positive photoresist (PR). The exposed resonator pattern is developed in a (TMAH)-based developer and then transferred to the sample using a boron trichloride (BCl_3) dry etch in an inductively coupled reactive ion etch (ICP-RIE) system, or through wet chemical etching using commercial aluminum etchant consisting of a mixture of phosphoric acid, acetic acid, and nitric acid.

Of particular concern for the samples that are etched in the ICP-RIE is the post-etch residue [38] composed of passivating non-volatile chlorinated byproducts [39] that form on the etched feature sidewalls [40]. These residues are important to dry etching as they have the positive role of creating anisotropic etch profiles. However, for aluminum, this etch residue is of concern because the chlorine free-radicals have the potential to corrode aluminum when the Al_yCl_x and Si_yCl_x compounds react with water to form hydrochloric acid [41].

Figure 6(a) shows the cross-sectional scanning electron microscopy (SEM) image and figure 6(b) shows the energy dispersive x-ray (EDX) spectroscopy map of a sample grown on a silicon substrate following pattern transfer using the ICP-RIE. The different colors in the EDX image indicate regions primarily composed of silicon (blue), aluminum (red), chlorine (green) and photoresist (purple). The chlorine containing compounds that are deposited on the etch feature sidewall are evident in both images. For the results presented here treatment of the post-etch residue is conducted entirely *ex-situ* after removal from the ICP-RIE tool. The impact of several mitigation strategies are discussed later.

Following removal of the post-etch residue the photoresist is stripped using a variety of procedures that include a series of hot chemical baths and ultrasonication to chemically and mechanically remove photoresist residue. Acetone is a common photoresist solvent that unfortunately leaves significant photoresist residue on the sample. However, most commercial photoresist strippers based on dimethyl sulfoxide (DMSO) and proprietary hydroxylamine-based solutions also attack aluminum. Alternatively NMP solvents do not attack aluminum the same way as commercial strippers. Unfortunately, NMP solvents are also not as effective in removing residues as commercial strippers, thus necessitating ultrasonication and long 6-hour soaks at 80°C with sequential solvent changes to insure the cleanest possible devices.

As shown in figure 7, the cleaning procedures often result in aluminum-etch-back and surface roughening. Aluminum-etch-back is apparent in the series of plan

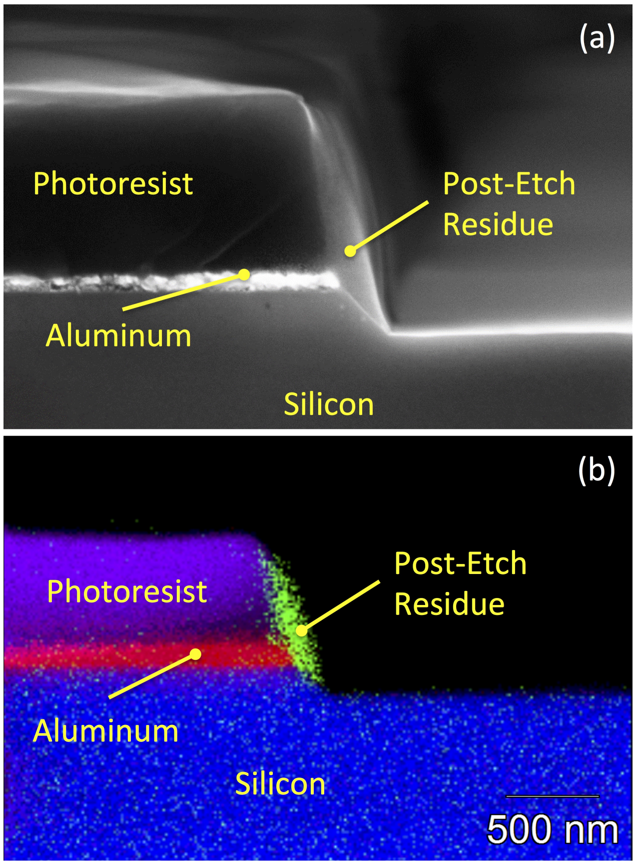

Figure 6. A (a) cross-sectional scanning electron microscopy image and (b) matching energy dispersive x-ray spectroscopy map of an aluminum film grown on a silicon substrate following pattern transfer using the ICP-RIE.

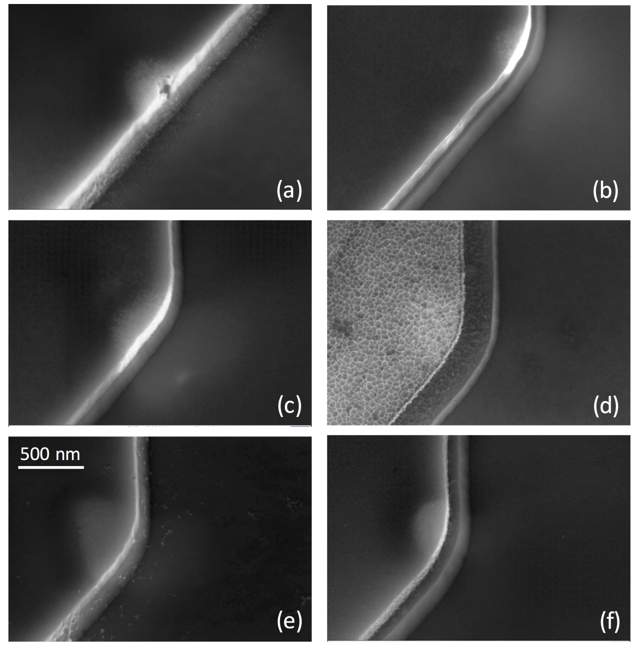

Figure 7. Accidental etch-back of aluminum from a variety of photoresist strip processes including: (a) NMP-based Solvent, () TMAH Developer dip + NMP-based Solvent, (c) Hot H_2O dip + NMP-based Solvent, (d) Hot H_2O dip + EKC256^{TM}, (e) Hot H_2O dip + AZ Kwik Strip and (f) Hot H_2O dip + EKC652^{TM}. All images are acquired at the same magnification

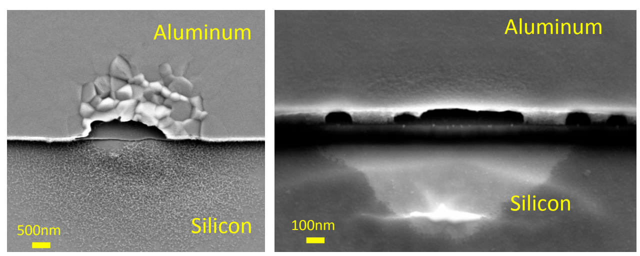

Figure 8. Accidental corrosion of aluminum sidewalls resulting from of chloride compounds contained in post-etch residues reacting with atmospheric moisture.

view SEM images because the samples are slightly over etched creating a silicon feature that is on the order of 100-nm-high, which acts as a convenient baseline of the receding aluminum edge. With the exception of (a) showing a NMP PR-strip, and (b) a quick 5-second dip in TMAH developer followed by the same NMP PR-strip the remaining procedures in figure 7 follow a hot H_2O dip to dissolve the post-etch sidewall residue followed by a PR-strip that consists of (c) NMP, (d) DuPont^{TM} SAC^{TM} EKC256^{TM}, (e) AZ Electronics Materials AZ Kwik Strip, or (f) DuPont^{TM} SAC^{TM} EKC652^{TM}. Variations in the sidewall etch-back, and sidewall roughness are evident. The moddled features in figure 7(c) are the result of excessive aluminum etching of the exposed aluminum surface.

6. Superconductor sidewall

With sufficient time, water adsorption from the atmosphere can impact the line edge defect density. The corrosion pits vary in morphology and size (50-500 nm) and to different degrees are observed in all aluminum sidewalls that are etched in the ICP-RIE for this study. Two representative sidewall defects are shown in the tilted-view SEM images in Figure 8.

The defects shown in Figure 8 show defects in epitaxial aluminum samples. Epitaxial aluminum tends to have smaller sidewall defects then polycrystalline aluminum evaporated in a conventional e-beam because the corrosion resulting from the post-etch residue is accelerated along grain boundaries causing the "mouse bites" shown here to become "worm trails".

A deionized (DI) water post-etch rinse washes away corrosive chlorine compounds [42, 43] and the impact of corrosion can be determined by monitoring the line edge defect density. For some samples a post-etch rinse in TMAH developer effectively removed the residue and resulted in an extremely low line edge defect density and noticeable aluminum-etch-back. While the generation rate of line edge defects are not directly transferable between labs the amount of time that the sample is exposed to atmosphere and the humidity in the lab both directly correlate to observable defect densities.

Fluorine-containing plasmas have also been used to quench the corrosiveness of the post-etch residue [42, 43]. Fluorine-plasmas are successful because the higher electronegative fluorine atoms replace chlorine in Al_yCl_x compounds. The resulting Al_yF_x products remain water soluble but they are not as reactive and do not generate the same corrosive compounds.

Here, plasma techniques are compared alongside a direct water rinse using a baseline recipe where the sample is exposed to atmosphere for 60s before being submerged into the DI water rinse followed by PR-strip. The first plasma process variation has a 40s exposure to atmosphere before the sample is under vacuum in the plasma tool where a low-energy CHF_3 and O_2 plasma followed by a DI water rinse and PR-strip. The last process variation also with a 40s transfer time but with an applied low-energy SF_6 + O_2 plasma which is also followed by DI water and PR-strip. The baseline process yields a sidewall defect density of 9.0 defects/mm, while the CHF_3 process produces sidewalls with 41.6 defects/mm, and the SF_6 process produces sidewalls with only 1.4 defects/mm.

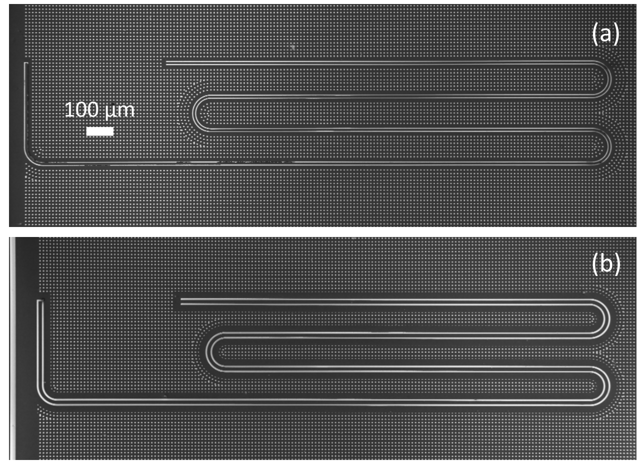

Figure 9. (a) SEM charge contrast imaging of photoresist contamination for a resonator with a cleaning procedure optimized using optical microscopy. (b) A similar resonator that is significantly cleaner following optimization using the SEM to detect the presence of photoresist residue.

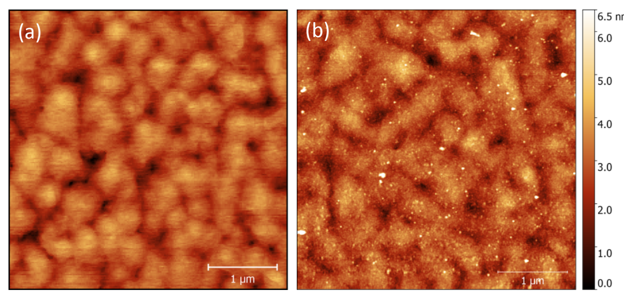

Figure 10. (a) Nanometer scale topography of as-grown epitaxial aluminum films and (b) nanoparticle defects deposited on the aluminum surface following resonator fabrication

7. Areal defects at air interfaces

While all samples look pristine under optical differential interference contrast microscopy that is routinely used to inspect devices in the cleanroom, charging contrast under low beam currents enable the SEM to be an effective tool to detect PR residue. Charge contrast electron imaging offers a more thorough screening protocol than optical micrograph. However, contamination concerns related to various samples imaged in most SEMs, carbon deposition on the sample from the field emission tip, and potential electron beam damage can lead to permanent sample damage seen by ghosting from imaged areas. This hindrance limits the SEM as a post-measurement inspection tool.

Areal defects coverage is examined on the superconductor surface and semiconductor clear field. Defects generally appear to be homogeneously distributed across the die surface in both the clear field and dark field regions. Specific characteristics of hardened photoresist residue near etched features, polishing contamination, and etch polymer by products are all readily discernible. Figure 9 illustrates process improvements resulting from routine use of charge-contrast imaging in the SEM to remove gross contamination from incomplete removal of photoresist residue. The most notable residue in figure 9(a) is along the left half of the bottom line and along the right-side bends in the regions that appear to break the higher intensity double lines from the spaces that define the coplanar waveguide.

In addition to the SEM, atomic force microscopy is used to determine the nanometer-scale particulate contamination. Figure 10 shows a small region of the mounded aluminum surface before (a) and after (b) resonator fabrication. There is consistent nanoparticle contamination of the devices surfaces with a particle density that is on the order of 50 μm^{-2}. Generally, the particle density is inhomogeneously distributed with mean particle radii of 15 $\pm$ 6 nm and mean particle height of 3.35 $\pm$ 0.8 nm.

8. Discussion

The intent of this study is to explore variations of resonator performance and identify categories of defect features that transcend processing recipes. While there are a few hero devices, there is significant scatter in the measured resonator performance across all process variations that were explored. Interestingly, the aluminum-etch-back that was noted in section 5 did not appear to negatively impact the internal quality factor of the superconducting resonators.

Through extensive inspection of numerous resonator chips and quantification of defect densities some correlations have begun to emerge. All resonators with losses less than 1x10^{-6} (internal quality factors above 1x10^{6}) also have low coverage areas of areal defects. However, the converse statement is not true, in that a low areal defect is not an independent and sufficient metric for high performance resonators. Alternatively, resonator performance is not found to correlate to line edge defect density. Further work is needed to definitively conclude that sidewall defects are not important to loss because of the strong spatial variations of the local electric field for the quarter-wave coplanar waveguides resonators studies here. One approach could be a complete mapping of the specific global location of each sidewall defect in order to determine a suitable participation factor for each defect.

The specific loss associated with the metamorphic epitaxial interface is currently unknown. However, this interface offers a canonical material to study as the periodic and highly ordered nature of this interface may allow the atom positions to be extensively simulated through molecular dynamic simulations [44], corroborated through atomic resolution STEM, or cross-sectional scanning tunneling microscopy (STM), and evaluated from an electronic structure perspective using DFT.

Large variability of the unsaturable background loss and variability indicate that tested devices are most likely process limited, particularly when the chip shows strong variation between neighboring devices. Only one particular photoresist was evaluated here, and it is possible that other photoresist materials may have other additives and accelerants that do not leave lossy residues.

9. Summary

Aluminum has been shown to be grown to a high degree of crystallinity and low contamination. Process artifacts continue to frustrate high coherency results due to the reactiveness of the aluminum material with photoresist solvents. Fabrication artifacts of high-Q resonators were identified through scanning electron microscopy. The observed artifacts may also plague aluminum Josephson junctions fabricated with e-beam lithography. Therefore, process optimization and improved inspection of resist residues is of utmost importance to the improvement of qubit lifetimes.

Acknowledgments

We gratefully acknowledge the resonator design provided by Dannielle Braje and Will Olver of MIT Lincoln Laboratory. The scanning transmission electron microscopy was performed at the Pacific Northwest National Laboratory (PNNL). PNNL is operated by Battelle for the U.S. Department of Energy, under contract DE-AC0576RL01830.

10. References

[1] A. Blais, R.-S. Huang, A. Wallraff, S. M. Girvin, and R. J. Schoelkopf. Cavity quantum electrodynamics for superconducting electrical circuits: An architecture for quantum computation. *Physical Review A*, 69(6):062320, 2004.

[2] J. Koch, T. M. Yu, J. Gambetta, A. A. Houck, D. I. Schuster, J. Majer, A. Blais, M. H. Devoret, S. M. Girvin, and R. J. Schoelkopf. Charge-insensitive qubit design derived from the Cooper pair box. *Physical Review A - Atomic, Molecular, and Optical Physics*, 76(4):1–19, 2007.

[3] R. Barends, J. Kelly, A. Megrant, A. Veitia, D. Sank, E. Jeffrey, T. C. White, J. Mutus, A. G. Fowler, B. Campbell, Y. Chen, Z. Chen, B. Chiaro, A. Dunsworth, C. Neill, P. O'Malley, P. Roushan, A. Vainsencher, J. Wenner, A. N. Korotkov, A. N. Cleland, and J. M. Martinis. Superconducting quantum circuits at the surface code threshold for fault tolerance. *Nature*, 508(7497):500–503, 2014.

[4] Z. Kim, B. Suri, V. Zaretskey, S. Novikov, K. D. Osborn, A. Mizel, F. C. Wellstood, and B. S. Palmer. Decoupling a Cooper-Pair Box to Enhance the Lifetime to 0.2 ms. *Physical Review Letters*, 106(12):120501, mar 2011.

[5] G. N. Gol'tsman, O. Okunev, G. Chulkova, A. Lipatov, A. Semenov, K. Smirnov, B. Voronov, A. Dzardanov, C. Williams, and R. Sobolewski. Picosecond superconducting single-photon optical detector. *Applied Physics Letters*, 79(6):705, aug 2001.

[6] J. M. Sage, V. Bolkhovsky, W. D. Oliver, B. Turek, and P. B. Welander. Study of loss in superconducting coplanar waveguide resonators. *Journal of Applied Physics*, 109(6):063915, 2011.

[7] A. Megrant, C. Neill, R. Barends, B. Chiaro, Y. Chen, L. Feigl, J. Kelly, E. Lucero, M. Mariantoni, P. J. J. O'Malley, D. Sank, A. Vainsencher, J. Wenner, T. C. White, Y. Yin, J. Zhao, C. Palmstrøm, and J. M. Martinis. Planar superconducting resonators with internal quality factors above one million Planar superconducting resonators with internal quality factors above one million. 113510:11–14, 2012.

[8] J. M. Martinis, K. B. Cooper, R. McDermott, M. Steffen, M. Ansmann, K. D. Osborn, K. Cicak, Seongshik Oh, D. P. Pappas, R. W. Simmonds, and C. C. Yu. Decoherence in Josephson Qubits from Dielectric Loss. *Physical Review Letters*, 95(21):210503, 2005.

[9] H. Paik and K. D. Osborn. Reducing quantum-regime dielectric loss of silicon nitride for superconducting quantum circuits. *Applied Physics Letters*, 96(7):072505, feb 2010.

[10] D. S. Wisbey, J. Gao, M. R. Vissers, F. C. S. da Silva, J. S. Kline, L. Vale, and D. P. Pappas. Effect of metal/substrate interfaces on radio-frequency loss in superconducting coplanar waveguides. *Journal of Applied Physics*, 108(9):093918, 2010.

[11] M. Sandberg, M. R. Vissers, J. S. Kline, M. Weides, J. Gao,

D. S. Wisbey, and D. P. Pappas. Etch induced microwave losses in titanium nitride superconducting resonators. *Applied Physics Letters*, 100(26):262605, 2012.

[12] C. M. Quintana, A. Megrant, Z. Chen, A. Dunsworth, B. Chiaro, R. Barends, B. Campbell, Y. Chen, I.-C. Hoi, E. Jeffrey, J. Kelly, J. Y. Mutus, P. J. J. O'Malley, C. Neill, P. Roushan, D. Sank, A. Vainsencher, J. Wenner, T. C. White, A. N. Cleland, and J. M. Martinis. Characterization and reduction of microfabrication-induced decoherence in superconducting quantum circuits. *Applied Physics Letters*, 105:062601, 2014.

[13] J. Wenner, R. Barends, R. C. Bialczak, Y. Chen, J. Kelly, E. Lucero, M. Mariantoni, A. Megrant, P. J. J. O'Malley, D. Sank, A. Vainsencher, H. Wang, T. C. White, Y. Yin, J. Zhao, A. N. Cleland, and J. M. Martinis. Surface loss simulations of superconducting coplanar waveguide resonators. *Applied Physics Letters*, 99(11):113513, 2011.

[14] M. R. Vissers, J. S. Kline, J. Gao, D. S. Wisbey, and D. P. Pappas. Reduced microwave loss in trenched superconducting coplanar waveguides. *Applied Physics Letters*, 100(8):2010–2013, 2012.

[15] A. Bruno, G. de Lange, S. Asaad, K. L. van der Enden, N. K. Langford, and L. DiCarlo. Reducing intrinsic loss in superconducting resonators by surface treatment and deep etching of silicon substrates. *Applied Physics Letters*, 106(18):182601, may 2015.

[16] W. A. Phillips. Two level states in glasses. *Reports of Progress in Physics.*, 50(February 1987):1689–1699, 1987.

[17] A. D. O'Connell, M. Ansmann, R. C. Bialczak, M. Hofheinz, N. Katz, E. Lucero, C. McKenney, M. Neeley, H. Wang, E. M. Weig, A. N. Cleland, and J. M. Martinis. Microwave dielectric loss at single photon energies and millikelvin temperatures. *Applied Physics Letters*, 92(11):112903, 2008.

[18] J. Gao, M. Daal, A. Vayonakis, S. Kumar, J. Zmuidzinas, B. Sadoulet, B. A. Mazin, P. K. Day, and H. G. Leduc. Experimental evidence for a surface distribution of two-level systems in superconducting lithographed microwave resonators. *Applied Physics Letters*, 92(15):152505, 2008.

[19] D. P Pappas, M. R Vissers, D. S Wisbey, J. S Kline, and J. Gao. Two Level System Loss in Superconducting Microwave Resonators. 21(3):871–874, 2011.

[20] A. M. Holder, K. D. Osborn, C. J. Lobb, and C. B. Musgrave. Bulk and surface tunneling hydrogen defects in alumina. *Physical Review Letters*, 111(6):1–5, 2013.

[21] L. Gordon, H. Abu-Farsakh, A. Janotti, and C. G. Van de Walle. Hydrogen bonds in Al2O3 as dissipative two-level systems in superconducting qubits. *Scientific Reports*, pages 1–5, 2014.

[22] S.-T. Lo, S.-W. Lin, Y.-T. Wang, S.-D. Lin, and C.-T. Liang. Spin-orbit-coupled superconductivity. *Scientific Reports*, 4, 2014.

[23] S.-W. Lin, Y.-H. Wu, L. Chang, C.-T. Liang, and S.-D. Lin. Pure electron-electron dephasing in percolative aluminum ultrathin film grown by molecular beam epitaxy. *Nanoscale Research Letters*, 10(1), 2015.

[24] C. H. L. Quay, Y. Chiffaudel, C. Strunk, and M. Aprili. Quasiparticle Spin Resonance and Coherence in Superconducting Aluminium. *arXiv*, 6:12, 2015.

[25] W. Chang, S.M. Albrecht, T. S. Jespersen, F. Kuemmeth, P. Krogstrup, J. Nygård, and C. M. Marcus. Hard gap in epitaxial semiconductor-superconductor nanowires. *Nature nanotechnology*, 10(3):232–6, 2015.

[26] T. W. Larsen, K. D. Petersson, F. Kuemmeth, T. S. Jespersen, P. Krogstrup, J. Nygård, and C. M. Marcus. Semiconductor-Nanowire-Based Superconducting Qubit. *Physical Review Letters*, 115(12):1–5, 2015.

[27] P. J Petersan and S. M Anlage. resonators : Comparison of methods. 84(6):3392–3402, 1998.

[28] J. Gao. The Physics of Superconducting Microwave Resonators Thesis by. *CIT PhD thesis*, 2008:1–141, 2008.

[29] B. Suri. Transmon qubits coupled to superconducting lumped element resonators, 2015.

[30] S. Novikov. Raman coherence effects in a superconducting Jaynes-Cummings system, 2015.

[31] R. Barends, J. Wenner, M. Lenander, Y. Chen, R. C. Bialczak, J. Kelly, E. Lucero, P. O'Malley, M. Mariantoni, D. Sank, H. Wang, T. C. White, Y. Yin, J. Zhao, A. N. Cleland, J. M. Martinis, and J. J. A. Baselmans. Minimizing quasiparticle generation from stray infrared light in superconducting quantum circuits. *Applied Physics Letters*, 99(11):113507, 2011.

[32] C. Song, M. P. DeFeo, K. Yu, and B. L. T. Plourde. Reducing microwave loss in superconducting resonators due to trapped vortices. *Applied Physics Letters*, 95(23):232501, 2009.

[33] H. Wang, M. Hofheinz, J. Wenner, M. Ansmann, R. C. Bialczak, M. Lenander, Erik Lucero, M. Neeley, a. D. O'Connell, D. Sank, M. Weides, a. N. Cleland, and J. M. Martinis. Improving the coherence time of superconducting coplanar resonators. *Applied Physics Letters*, 95(23):233508, 2009.

[34] D. Ali and C. J. K. Richardson. Reflection high-energy electron diffraction evaluation of thermal deoxidation of chemically cleaned Si, SiGe, and Ge layers for solid-source molecular beam epitaxy. *Journal of Vacuum Science & Technology A: Vacuum, Surfaces, and Films*, 30(6):061405, 2012.

[35] Y Miura, S Fujieda, and K Hirose. Single-crystal Al growth on Si (111) by low-temperature molecular beam epitaxy. *Applied physics letters*, 62(15):1751, 1993.

[36] F. K. Legoues, W. Krakow, and P. S. Ho. Atomic structure of the epitaxial Al–Si interface. *Philosophical Magazine A*, 53(6):833–841, jun 1986.

[37] A. Uemura, A. Ohkita, H. Inaba, and S. Hasegawa. Effects of Si reconstruction on growth mode in A1 / Si (111) studied by scanning tunneling microscopy. 358:825–829, 1996.

[38] D. W. Hess. Plasma etch chemistry of aluminum and aluminum alloy films. *Plasma Chemistry and Plasma Processing*, 2(2):141–155, jun 1982.

[39] D. A. Danner. Plasma Etching of Aluminum. *Journal of The Electrochemical Society*, 134(3):669, mar 1987.

[40] J. Proost. Chemical and Electrical Characterization of the Interaction of BCl_3/Cl_2 Etching and CF_4/H_2O Stripping Plasmas with Aluminum Surfaces. *Journal of The Electrochemical Society*, 146(11):4230, nov 1999.

[41] I. W. Rangelow. Reactive ion etching for microelectrical mechanical system fabrication. *Journal of Vacuum Science & Technology B: Microelectronics and Nanometer Structures*, 13(6):2394, nov 1995.

[42] N. Parekh. Cl Level Effects on Corrosion for Various Metallization Systems. *Journal of The Electrochemical Society*, 137(7):2199, jul 1990.

[43] S. Mayumi. Post-Treatments for Reactive Ion Etching of Al-Si-Cu Alloys. *Journal of The Electrochemical Society*, 137(8):2534, aug 1990.

[44] G. Pilania, B. J Thijsse, R. G Hoagland, I. Lazić, S. M Valone, and X.-Y. Liu. Revisiting the Al/Al_2O_3 interface: coherent interfaces and misfit accommodation. *Scientific reports*, 4:4485, 2014.